2. *Proprioceptive feedback modulates motor cortical tuning during human brain-machine interface control*

2.1 Abstract

Loss of proprioception is known to severely impair motor control, but the neural mechanisms by which proprioception aids in the planning and execution of visually guided movements are not well understood. We investigated the impact of providing proprioceptive feedback to a human subject with tetraplegia and intact sensation who was implanted with two 100-channel micro-electrode arrays in primary motor cortex (M1). BMI-assisted reach performance was highly dependent on the feedback sources provided during decoder training; if a decoder was trained with vision alone, adding proprioceptive feedback during a reach task degraded reach performance. The inability to mismatch decoder and task feedback conditions arises from a shift in M1 velocity tuning between the visual (V) and visual+proprioceptive (VP) feedback conditions. The VP condition was also marked by decreased modulation depth and increased variability of M1 velocity tuning, which resulted in degraded BMI-assisted reach performance. Because we do not believe that proprioception fundamentally degrades motor control in healthy individuals, we propose that M1 encodes proprioceptive information with dynamics unknown to our BMI decoder. We show evidence that M1 activity in the VP condition is better modeled with the inclusion of a smooth, time-dependent, modulator that is shared amongst the neural population. Our encoding model that includes this modulator improves M1 tuning the most when the subject receives somatosensory feedback, suggesting the modulator captures shared variability from somatosensory inputs to M1. Together, our results suggest that new decoders will need to

be developed for closed-loop BMIs that make efficient use of natural or surrogate somatosensory information.

2.2 Introduction

Complex limb movements like reaching and grasping are closed-loop motor programs that integrate feedback from multiple sensory modalities [73, 74]. A person attempting to grasp a cup must first visually locate the cup, plan a movement trajectory to the target [75], and issue that motor command through a pattern of motor cortex (M1) activity [76]. The motor command is read out by the spinal cord and executed by muscle motor neurons [73]. As the reach progresses, the person receives both visual and proprioceptive feedback to guide the movement and correct for perturbations [77]. Accordingly, motor control degrades significantly in human subjects with afferent pathway damage that results in the loss of proprioceptive information [78, 79, 80]. Recent studies have confirmed that somatosensory cortex (S1) communicates directly to M1 via monosynaptic projections that are capable of driving motor behavior [81, 82].

Brain machine interfaces (BMIs) restore motor function in patients with spinal cord injuries and damaged efferent pathways by transforming M1 activity to a control signal for a cursor or robotic arm [83]. Despite the known importance of proprioceptive information for upper extremity control, most current BMI implementations rely exclusively on visual feedback [84]. We had the rare opportunity to investigate the differential effects of providing proprioceptive feedback to a human subject during her BMI control. The subject, who has tetraplegia but intact sensation, used a BMI in which an exoskeleton moved her own arm congruently with a virtual arm or robotic arm. She thus received proprioceptive information from her muscle and tendon stretch receptors [85] and tactile information from the interaction between her arm and the exoskeleton [86].

Unlike the results of a previous study on proprioceptive feedback during non-human primate BMI control [87], our subject's performance of a BMI-assisted reaching task degraded when we allowed a decoder trained only with visual feedback to leverage the subject's proprioceptive signals. More generally, the feedback sources provided during decoder training and online BMI control could not be mismatched without a degradation of reach performance. This behavioral

observation suggested that proprioception altered the decoder's known mapping between neural activity and kinematics. Analysis of neural activity confirmed that additive proprioceptive feedback shifted the velocity tuning curves of recorded M1 channels. Proprioceptive feedback also caused a decrease in the modulation depth of M1 velocity tuning curves, making neural activity non-exchangeable between reaches guided with somatosensory feedback and those guided with vision alone.

Contrary to the intuition that additive somatosensory feedback could only aid BMI performance, our subject's BMI assisted reach control degraded with online proprioceptive feedback, even when the decoder was trained using proprioception. The neural signature of this behavioral effect was reduced signal to noise ratio of M1 velocity tuning during trials when the patient had somatosensory feedback. This manifested as (1) a decrease in the modulation depth of velocity tuning curves, (2) an increase in the trial-to-trial variability of velocity tuning curves, and (3) an increase in the noise correlations of M1 activity.

Because we do not believe that proprioceptive information fundamentally degrades motor control in healthy individuals, we propose that M1 encodes proprioceptive information in ways incongruous with the simple endpoint velocity tuning leveraged by current BMI decoders. After the effects of velocity tuning were removed, neural activity in the proprioceptive feedback condition contained gain fluctuations that were coordinated across broad subpopulations of recorded M1 channels. The coordinated fluctuation of neural activity that we observed in the proprioceptive feedback condition is consistent with observations that M1 may integrate information from large regions of S1 [88]. Moreover, several recent studies have uncovered low-rank co-fluctuations of neural activity in cortex [55, 22, 23].

To account for co-fluctuations that might drive the M1 population when the subject had proprioceptive feedback, we developed a novel M1 encoding model in which the spiking activity of each recorded M1 channel is a function of channel-specific tuning for endpoint velocity and a time-varying waveform of activity that is shared across the M1 population. The addition of a global gain-modulating waveform improves velocity tuning in the proprioceptive feedback condition. We therefore propose that S1 activity might be encoded as a shared wave of activity that broadly modulates the gain of M1 neurons. BMIs seeking to make efficient use of natural or surrogate somatosensory feedback may need to account for such shared modulators.

2.3 Methods

The experimental methods that follow will be described in more detail in a forthcoming publication by Gaunt et al.

2.3.1 Study participant and regulations

The subject was a 52 year old woman with a diagnosis of spinocerebellar degeneration without cerebellar involvement, manifesting as complete tetraplegia with generally intact afferent innervation. While the subject did have some mild sensory deficits and hypersensitivity, clinical testing confirmed that her proprioception was robust enough to give her appropriate feedback.

The subject provided informed consent verbally for study participation, with documents signed by her legal proxy. The study was carried out under approval from the Institutional Review Boards of the University of Pittsburgh, and the Space and Naval Warfare Systems Center Pacific. Implanted devices were granted Investigational Device Exemption by the US Food and Drug Administration. The trial is registered on clinicaltrials.gov under identifier NCT01364480.

2.3.2 Behavioral tasks

The subject was trained to control either an adjacent, free-standing prosthetic arm (modular prosthetic limb [MPL], Johns Hopkins University, Applied Physics Laboratory, Baltimore, MD, USA), or a virtual representation of that arm, in a two-dimensional workspace. The subject completed two tasks that tested her BMI-assisted motor control. The first, a line-crossing (LC) task, required the subject to move the MPL medial-laterally across parallel lines spaced 20 cm apart as many times as possible in a 60 s period (Figure 2.1a). We used the number of line crossings achieved in the 60 s trial to measure the extent to which the subject could effectively control the MPL. Though the task was one-dimensional, MPL control was two-dimensional in the coronal plane.

The second task, a 2D pursuit (2DP), required the subject to move a virtual arm to one of five on-screen targets in the following positions of the coronal plane: center, above-center, left-of-center, right-of-center, or below-center (Figure 2.2a). The subject received a visual signal of

the target that was to be pursued before the movement onset cue. The subject did not have to return to the center target after each reach.

The subject completed the two tasks described above using the typical BMI control paradigm of exclusively visual feedback (V) and a paradigm in which she received simultaneous visual and proprioceptive feedback (VP). In the VP paradigm, the subject's own arm was placed in an upper extremity exoskeleton (Armeo Power, Hocoma, Switzerland) and moved congruently with the MPL or virtual arm. In a small subset of initial LC task trials with VP feedback, prior to the introduction of the exoskeleton, an experimenter manually moved the subject's arm congruently with the MPL. The number of line crossings achieved in the VP condition did not differ significantly between trials in which the arm was moved manually and trials in which the arm was moved with an exoskeleton. The subject was always unable to view her own moving arm in the VP paradigm, disallowing multiple points of visual attention.

2.3.3 Electrophysiology

The subject had two 100-channel microelectorde arrays (4 x 4 mm^2 footprint, 1.5 mm shank length, Blackrock Microsystems, Salt Lake City, UT, USA) implanted into the somatotopic region of left M1 responsible for right arm and hand control [89]. The experiments analyzed in this study began 11 months post-implantation and continued until two years post-implantation. Signals from up to 192 microelectrodes were recorded. Each microelectrode recorded intracortical neuron depolarization using the NeuroPort data acquisition system (Blackrock Microsystems, Salt Lake City, UT, USA). Several parameters were saved from these depolarizations, including threshold crossings, timing and action potential waveform snippets. Due to the low firing rates observed in the recorded M1 activity, action potentials were not sorted to distinguish signals generated by individual neurons. Therefore, the neural data recorded on each channel of the array, which were used for decoding and all post-hoc analysis, may represent the activity of multiple neurons. Threshold crossing times were collected into 30 ms time bins to create a vector of spike counts $s_i(t)$ for each of the N total recorded channels.

2.3.4 Online decoding

Commands from motor cortex produce unique combinations of spiking activity [76]. The control scheme for a BMI thus requires a map between spiking activity and the kinematics of the MPL or virtual arm. To train the BMI decoder, the subject observed a computer program performing the 2DP task. She was visually cued to the appropriate reach target and then instructed to imagine performing the reach while she observed the virtual arm's movement. The spike count $s_i(t)$ of each recorded neural channel i was smoothed with a low pass filter in which the kernel was an exponential function of 450 ms width. A square root transform was performed on the smoothed vector to stabilize variance. Each channel's resulting firing rate vector $f_i(t)$ was then mapped to the virtual arm's movement velocity according to

$$f_i(t) = \beta_{i0} + \beta_{i1}v_x(t) + \beta_{i2}v_y(t) + \varepsilon_i(t) \tag{2.1}$$

where $v_x(t)$ and $v_y(t)$ are vectors of the x and y velocity of the virtual arm over the reach duration. In matrix form, this relationship is expressed as

$$F = VB + \varepsilon \tag{2.2}$$

where F is the $T \times N$ matrix of all channel firing rate vectors $f_i(t)$ over the total trial duration T, V is a T x 3 column matrix defined by $[\vec{1}, v_x(t)^\top, v_y(t)^\top]$, B is the $3 \times N$ matrix of regression coefficients $[\vec{\beta_0}^\top, \vec{\beta_1}^\top, \vec{\beta_2}^\top]$, and ε is the matrix of channel residuals $\sim \mathcal{N}(0, \sigma^2)$.

The maximum likelihood estimate of B with ridge regression regularization is:

$$\hat{B} = (V^T V + \lambda \mathbb{I})^{-1} V^T F \tag{2.3}$$

where λ is the regularization parameter optimized to minimize the prediction risk of F and $\mathbb{I}$ is a 3×3 identity matrix.

The mapping between firing activity and kinematics in Equation (2.2) was then inverted to predict the subject's reach intent during the behavioral tasks according to:

$$V = FW + \varepsilon \tag{2.4}$$

where the weight matrix W can be computed by taking the Moore-Penrose Pseudoinverse of $\hat{B}$ in Equation (2.4). Additional details about the decoder can be found in Collinger et al. [89] and Wang et al. [90].

We computed the mapping between velocity information and firing activity that is described above for two different feedback paradigms during 2DP training: one paradigm in which the subject had only visual feedback of the virtual arm (V), and one in which the subject had both visual and proprioceptive feedback (VP), provided by the exoskeleton. This resulted in two sets of decoder parameters, which we will refer to as W_V and W_{VP}.

2.3.5 Reach analysis

In the LC task, we evaluated the subject's ability to control her reaching movements by three metrics: (1) the number of line crossings she achieved in a 60 s period, (2) the mean path length per line crossing, and (3) the variance of the reach in the anterior-posterior dimension, which was the dimension of control orthogonal to the LC goal. In the 2DP task, we evaluated the subject's performance by the number of reaches that were successfully terminated at the designated target within a 3 s period. For each task, reach trajectories were smoothed with a Gaussian filter of width 200 ms. Kinematic observations were pooled across trials, and a two-way ANOVA with post hoc t-tests was used to determine whether performance differed across the feedback and decoder conditions.

2.3.6 Post-hoc tuning curve analysis

Our reach analysis suggested that the structure of the neural activity differed in the V and VP conditions. We therefore conducted a post-hoc analysis of M1 tuning, to compare M1 activity structure in the V and VP conditions. Previous studies have demonstrated that the preferred velocity directions of M1 neurons shift with prolonged BMI decoder in ways that optimize the movement readout of the decoder [91, 92, 93]. We wanted to study the natural structure of M1 activity in the V and VP feedback conditions, without the conflating influence of optimized decoder readout. We therefore focussed our analysis of M1 activity on the neural data recorded during the 2DP decoder training, when the subject imagined movement rather than affecting it with the neuroprosthetic.

The majority of recorded channels had very low, sub-5 Hz firing rates and Fano Factors of approximately 1. We therefore chose to re-analyze neural data using each channel's un-smoothed vector of spike counts $s_i(t)$. We fit new tuning curves, or mappings between each channel's spiking activity and the velocity of the virtual arm, according to the following Poisson regression:

$$\log(s_i(t)) = \beta_{i0} + \beta_{i1} v_x(t) + \beta_{i2} v_y(t) + \varepsilon_i(t) \tag{2.5}$$

where $v_x(t)$ and $v_y(t)$ are the x and y coordinates of the velocity vector $v(t)$ standardized by its Euclidean norm. Equation (2.5) can be restated as Equation (2.6), the cosine form of tuning commonly used to describe the velocity preferences of M1 neurons [76]:

$$\log(s_i(t)) = \alpha_{i0} + \alpha_{i1} \cos(\theta(t) - \theta_{iPD}) + \varepsilon_i(t) \tag{2.6}$$

where θ is the angle formed by the velocity vector $[v_x, v_y]$ and θ_{iPD} is the preferred direction of channel i. Channels for which the velocity tuning curve in Equation 2.6 did not explain significantly more variance than the spike count mean were excluded from all analyses that follow (Chi-squared test, $p < 0.05$ with Bonferroni correction).

The modulation depth of a tuning curve measures the strength of a channel's preference for θ_{iPD} over other velocity directions. Modulation depth was calculated as the difference between the channel's maximum and minimum fitted spike count standardized by the channel's maximum fitted spike count, and therefore always takes a unitless value between 0 and 1. Variability about fitted curves, or model dispersion, was estimated using the ratio between the residual deviance and the residual degrees of freedom of the model.

Correlations in the noise of the neural population describe the co-activity of channels once the effect of velocity tuning has been removed. Noise correlations were computed using the N x N pairwise correlation matrix Σ of each channel's tuning curve residual vector, $\varepsilon_i(t)$. Relatedly, the *mood* of the M1 population–which characterizes population-wide co-fluctuations of noise over time–was calculated by averaging residual vectors $\varepsilon_i(t)$ across all N channels. We characterized the degree to which a channel's non-velocity-tuned activity was coupled to the population mood by computing the Pearson correlation between the channel's residuals $\varepsilon_i(t)$ and the mood function.

2.3.7 A new, shared gain model of M1 tuning

Our post-hoc analysis of tuning curves revealed large co-fluctuations of noise in the VP condition. We therefore developed a novel model of M1 tuning in which we appended a time-varying signal that was shared amongst the neural population to the tuning model in Equation (2.5). The resulting tuning structure is described by the generalized additive model [94] below,

$$\log(s_i(t)) = \beta_{i0} + \beta_{i1}v_x(t) + \beta_{i2}v_y(t) + \gamma(t) + \varepsilon_i(t) \tag{2.7}$$

where $\gamma(t)$ is a single smooth function of time that is shared by all channels. Note that though $\gamma(t)$ is the same for every channel, the degree of coupling that each channel i has to the shared waveformform is allowed to vary through the intercept value β_{i0}. Also note that due to the log link function used in Poisson regression, $\gamma(t)$ modulates the gain of a channel's velocity tuning.

Equation (2.7) requires that all N channels be fit simultaneously. Our model design matrix $H \in \mathbb{R}^{TN \times (KN+1)}$ has the form

$$H = \begin{pmatrix} \tau_1 & V_1 & 0 & \dots & 0 \\ \tau_2 & 0 & V_2 & \ddots & \vdots \\ \vdots & \vdots & \ddots & \ddots & 0 \\ \tau_N & 0 & \dots & 0 & V_N \end{pmatrix}, \tag{2.8}$$

where $V_i \in \mathbb{R}^{T \times K}$ is the matrix of K kinematic covariates to which each channel i is fit independently:

$$V_i = V = [\vec{1}, v_x(t)^\top, v_y(t)^\top], \tag{2.9}$$

and $\tau_i \in \mathbb{R}^{T \times 1}$ is a vector of time indices to which our shared function $\gamma(t)$ is simultaneously fit across each channel i:

$$\tau_i = \tau = [1, 2, ..T]^\top. \tag{2.10}$$

Because we did not have prior knowledge about the form of the shared gain waveform, we sought a smooth, flexible, and non-parametric transformation of the shared time index vector. We chose to model the gain waveform as a 1st degree local linear regression on the time index vector, corresponding to a kernel smoother in which each kernel is fitted with a weighted least

squares linear regression between spiking activity and time index. Briefly, the general form of a local linear linear estimator $\hat{r}(x)$ of response variable Y with standard, Gaussian error distribution is

$$\hat{r}(x) = \sum_i \ell_i(x) Y_i$$

$$\ell(x)^\top = e_1^\top (X_x^\top W_x X_x)^{-1} X_x^\top W_x$$

$$X_x = \begin{pmatrix} 1 & x_1 - x_0 \\ 1 & x_2 - x_0 \\ \vdots & \vdots \\ 1 & x_n - x_0 \end{pmatrix}$$

$$e_1 = (1, 0, ..., 0)^\top$$

$$W_x = w_i(x_0) \mathbb{I} \tag{2.11}$$

Our regression model is for a response variable with Poisson distributed error and requires a link function. See Fan et al. [95] for a generalized linear model treatment of local polynomial regression.

We used cross validation to select the kernel width of the smoother for each training session dataset independently. The kernel width selected by cross validation was always a physically interpretable number of time steps less than T, the duration of all reaches in the training session, despite that the total length of the time index column of H was TN. We fit the full model described by Equation (2.7) with the open source **gam** package in the scientific computing language **R**. The **gam** package fits generalized additive models using the backfitting algorithm [94], in which the partial residuals of each of the additive model terms are fit iteratively until the residual sum of squares of the full model satisfies the convergence criterion.

We evaluated the fit of the shared gain tuning model using the *deviance*, a scaled version of the log-likelihood ratio of two nested models. The total deviance of the shared gain model, which is equivalent to adjusted R^2, expresses the log-likelihood ratio between the shared gain model fit and a null model fit, where the null model is the mean spike count of a channel. We can also calculate the proportion of deviance explained by the added gain term $\gamma(t)$. This is equivalent to computing the log-likelihood ratio between the Equation (2.7) and Equation (2.5)

model fits.

2.4 Results

2.4.1 M1 tuning changes in the presence of proprioceptive feedback

The subject first completed the 2DP decoder training with V and VP feedback, resulting in two sets of decoding parameters, W_V and W_{VP}. Each set of decoding parameters was used to perform the LC task, and the subject received either V or VP online feedback on a given trial (Figure 2.1a). This protocol allowed us to test the effect of mismatching decoder training protocol and task feedback condition. For example, the subject could perform the LC task with online VP feedback, even if the W_V decoder was being used to drive the movement of the MPL.

The subject's LC task performance degraded when we mismatched the decoder training protocol and the online task feedback. When using the W_V decoder, she completed significantly more line crossings in the V than the VP condition ($p < 0.05$), with an average of 27.9 ± 3.57 and 22.5 ± 3.37 line crossings (mean $\pm$ 1 SE, across all recording sessions) for the V and VP feedback conditions, respectively (Figure 2.1b). When using the W_{VP} decoder, she completed more line crossings in the VP (26.8 ± 3.01) than the V (24.3 ± 4.08) condition, though this effect was not significant, (mean $\pm$ 1 SE, across all recording sessions).

The quality of the subject's reaches during the LC task also degraded visibly when we mismatched the decoder training protocol and the online task feedback (Figure 2.1c-d). When the subject used the W_V decoder, the mean reach path length per line crossing was significantly smaller ($p < 0.01$) in the V (0.52 ± 0.009 m) than the VP (0.69 ± 0.045 m) condition (mean $\pm$ 1 SE, across all recording sessions). When the subject used the W_{VP} decoder, the mean reach path length per line crossing was significantly smaller ($p < 0.05$) in the VP (0.62 ± 0.019 m) than the V (0.67 ± 0.024 m) condition (mean $\pm$ 1 SE, across all recording sessions). The subject's decreased ability to control the reach when decoder training protocol and the online task feedback were mismatched was even more obvious when we analyzed the variance of her reaches in the task irrelevant dimension. Though the line crossing task was essentially one-dimensional, the subject had two-dimensional control of the MPL in the coronal plane. Optimal task performance would show negligible reach variability in the superior/inferior dimension, which was
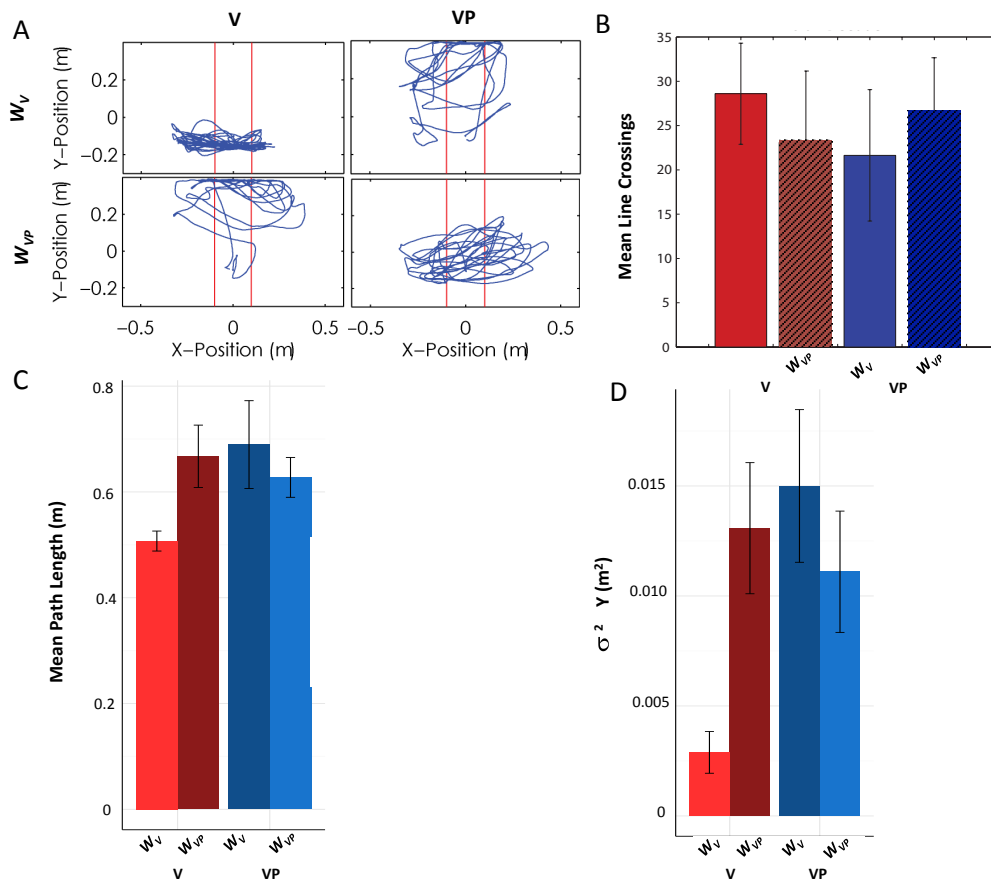
Figure 2.1: BMI-assisted 1D reaches suffer from proprioceptive feedback **(a)** Overhead view of single-trial reach trajectories in the BMI-assisted line-crossing task using the decoder training with vision alone (WV) or vision+proprioception (WV P) decoder. Online reach feedback was visual (V) or visual and proprioceptive (VP). **(b)** Mean number of line-crossings achieved in a 60 s period, pooled across four days of trials containing 5 runs each. Error bars represent 95% CIs. **(c)** Mean path length per line crossing, pooled across the same 4 days. Error bars represent 95% CIs. **(d)** Mean variance of reach in the task irrelevant dimension, pooled across the same four days. Error bars represent 95% CIs.

orthogonal to the LC goal. Variance in the task irrelevant dimension was significantly smaller ($p < 0.01$) in the V (0.0026 ± 0.00045 m^2) than the VP (0.015 ± 0.0018 m^2) condition when the subject used the W_V decoder (mean $\pm$ 1 SE, across all recording sessions). Similarly, variance in the task irrelevant dimension was significantly smaller ($p < 0.05$) in the VP (0.0118 ± 0.0011 m^2) than the V (0.0129 ± 0.0016 m^2) condition when the subject used the W_{VP} decoder (mean $\pm$ 1 SE, across all recording sessions).

The subject then completed the 2DP task (Figure 2.2a) with same 2×2 experimental block design that tested the interaction effects between decoder parameters and online task feedback
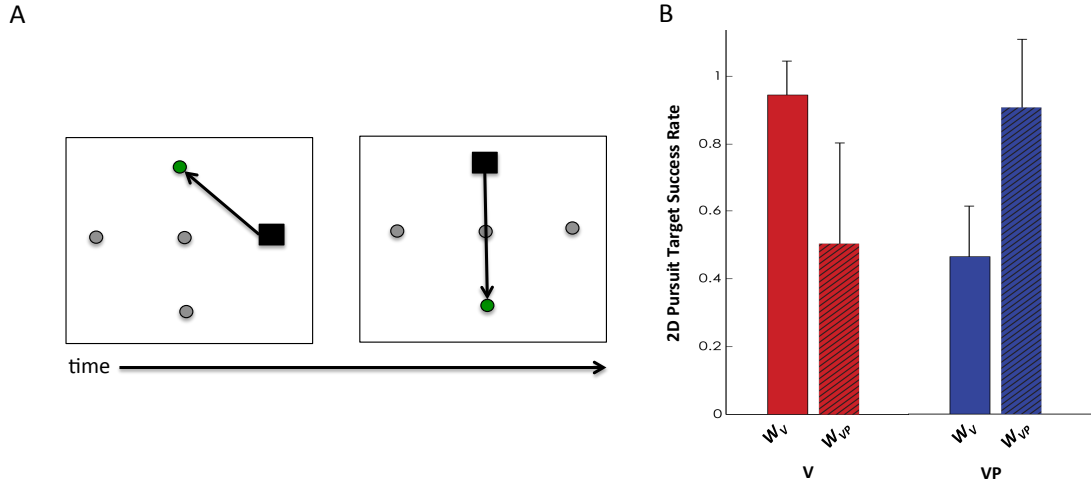
Figure 2.2: BMI-assisted 2D reaches suffer from mismatched feedback conditions **(a)** Schematic of the 2D pursuit task. The black box represents the virtual arm, the circles represent the 5 possible targets, and the green circle represents the target the subject was cued to pursue. Examples of 2 consecutive reaches are shown. **(b)** Average proportion of targets at which the subject successfully terminated a reach within a 3 s period during a single iteration of the 2D pursuit task, which contained approximately 30 reaches. Results are pooled across 5 iterations of the task in each condition. Error bars represent 95% CIs.

conditions. We quantified proficiency in the 2DP task by the fraction of times the subject successfully terminated a reach at the correct target within a 3 s period. As in the LC task, performance degraded significantly ($p < 0.01$) when we mismatched the decoder training protocol and the online task feedback (Figure 2.2b).

The subject's motor performance when using the W_V and W_{VP} decoders was not exchangeable, suggesting that the structure of M1 activity changed between the V and VP conditions. BMI decoders rely on a mapping between reach velocity and M1 activity, and failure of a BMI decoder necessitates that the mapping is no longer valid. We therefore sought to understand the difference between the map from kinematics to M1 activity in the V and VP conditions. Visualizations of channel firing rates as a function of velocity direction for the LC task revealed stable velocity tuning curves over multiple trials within a feedback condition, but not across feedback conditions (Figure 2.3a).

Tuning curves from the LC or 2DP tasks, when the subject affected movement with the BMI, might be a conflation of M1's natural tuning structure and a tuning structure M1 has learned to optimize the output a specific decoder [91, 92, 93]. We wished to investigate the natural state
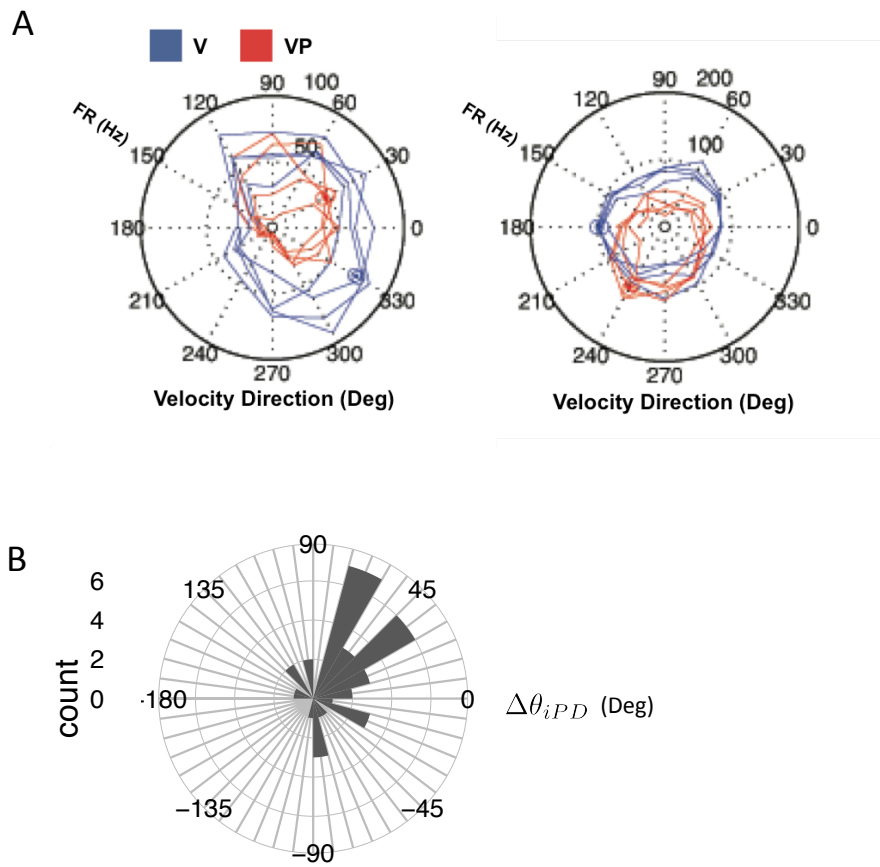
A

B

Figure 2.3: Shifts in preferred direction. **(a)** Firing rate as a function of velocity direction for 2 example M1 channels. Each curve represents one repetition of the line-crossing task, and four repetitions of the task are shown. Curves are stable within reach feedback type, but not across feedback types. Left: An example channel for which VP decreases modulation depth of velocity tuning. Right: An example channel for which there is a stable shift in θ_{iPD} between feedback conditions. **(c)** Distribution of the shift in preferred direction, $\Delta\theta_{iPD}$, between the V and VP conditions on the matched day.

of M1 velocity tuning in the V and VP conditions, not those potentially imposed by the W_V or W_{VP} decoder. To do this, we re-fit velocity tuning curves to the M1 activity recorded during W_V and W_{VP} training sessions, when the subject merely imagined movement. Our experiments were not designed with the purpose of detecting a shift in M1 velocity tuning between feedback conditions. This unexpected finding was only uncovered once we completed a more detailed analysis of the neural data, which was after the date when we were required to explant the subject's microelectrode arrays. Our data therefore contains only one session in which W_V and W_{VP} training was completed on the same day. This is the only day for which we can be reasonably certain that the activity of a channel i will reflect the activity of the same neuron or group of neurons for both the V and VP conditions. On this day, which we will henceforth refer
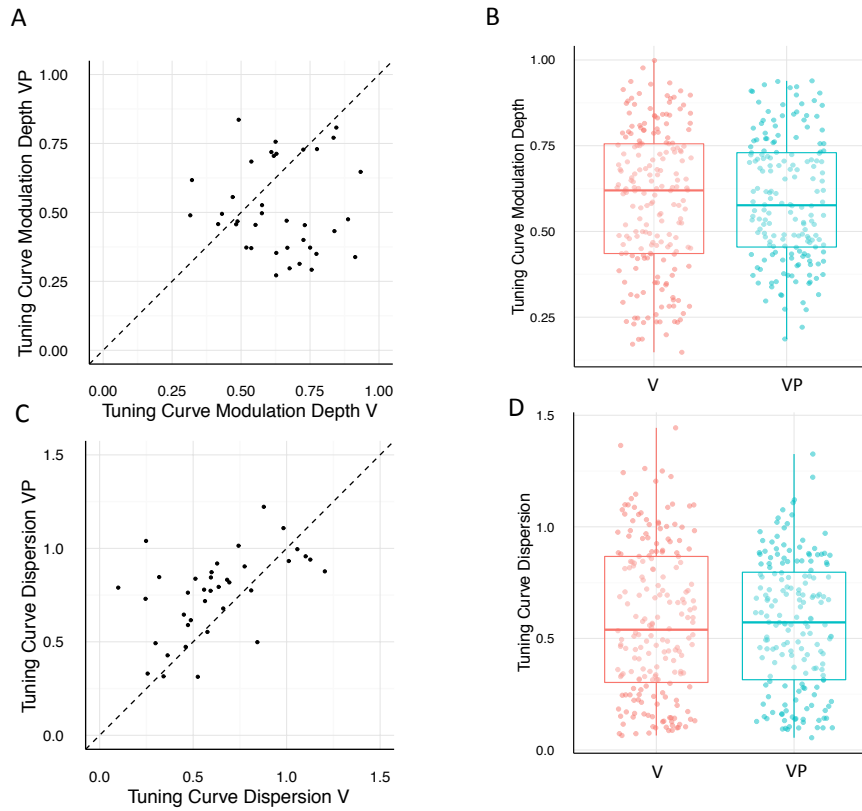
Figure 2.4: M1 responses have diminished velocity tuning in the VP condition. **(a)** Modulation depth of velocity tuning curves for each channel i on the paired day, compared across the V and VP conditions. Channels have larger modulation depth in the V condition. **(b)** Modulation depth of all analyzed channels in the V and VP conditions, pooled across four training sessions per condition. **(c)** The dispersion, or variability, about each channel i's fitted velocity tuning curve on the paired day, compared across the V and VP conditions. Velocity tuning is more variable in the VP condition. **(d)** Tuning curve dispersion of all analyzed channels in the V and VP conditions, pooled across the four training sessions per condition.

to as the *paired day*, there were roughly 60 tuned channels in the W_V and $W_V P$ conditions, and 37 channels that were tuned in both conditions. Of these 37 channels, $59.4 \pm 9\%$ (mean $\pm$ 1 SE, bootstrap) of channels exhibited $\geq 45°$ changes in the preferred velocity direction θ_{PD} (Eq. (2.5)) between the V and VP conditions (Figure 2.3b). The VP condition was also associated with a decrease in the modulation depth of the fitted velocity tuning curve. On the paired day, $37.8 \pm 6\%$ (mean $\pm$ SE, bootstrap) of channels exhibited $\geq 20\%$ decrease in modulation depth in the VP condition (Figure 2.4a).

33

2.4.2 Proprioceptive input results in shallower and more variable velocity tuning curves

One would intuitively think that additional sources of sensory feedback could only improve BMI performance. Contrary to that intuition, the quality of the subject's reaches in the LC task degraded strikingly in the VP condition even when the subject used the W_{VP} decoder. Reach variance in the task irrelevant dimension was significantly larger ($p < 0.001$) in the condition where VP feedback was provided to a W_{VP} decoder than the condition when V feedback was provided to a W_V decoder (Figure 2.1d). The mean path length per line crossing was also significantly greater ($p < 0.001$) in the condition where VP feedback was provided to a W_{VP} decoder than the condition when V feedback was provided to a W_V decoder (Figure 2.1c).

The behavioral result explained above cannot be accounted for by a shift in velocity tuning between the V and VP conditions, because we removed the effect of mismatched decoders. Instead, the behavior indicates that M1 activity must be less tuned to endpoint velocity in the VP condition (without accounting for latent sources of shared variability). We fit neural data from W_V and W_{VP} with velocity tuning models described by Equation 2.5 and calculated the dispersion of those tuning models, a measure of the spike count variability about the fitted tuning curve. Though both V and VP tuning curves had sub-Poisson variability (dispersion < 1), dispersion was larger in the VP than the V condition. This was true to significant effect for the paired day training sessions (Figure 2.4c), for which we could directly compare the V and VP tuning curves of a channel i with confidence that the same neurons were being recorded in the two feedback conditions. VP tuning curves had greater dispersion on average when channel statistics were pooled across all four training sessions of each feedback type, but this effect was not significant (Figure 2.4d). As discussed previously, the modulation depth of tuning curves was also smaller in the VP condition than the V condition. Tuning curves were therefore broader (i.e., more overlapping) and more variable in the VP condition, which would result in more variable BMI output for a given reach intention.

Finally, we observed that neural data in the VP condition contained co-fluctuations of activity that were not tuned to velocity and that were shared by large subpopulations of channels. Correlations in noise–the neural activity once the mean effects of the velocity tuning were removed–were greater in the VP than the V condition on the paired day, when there is high
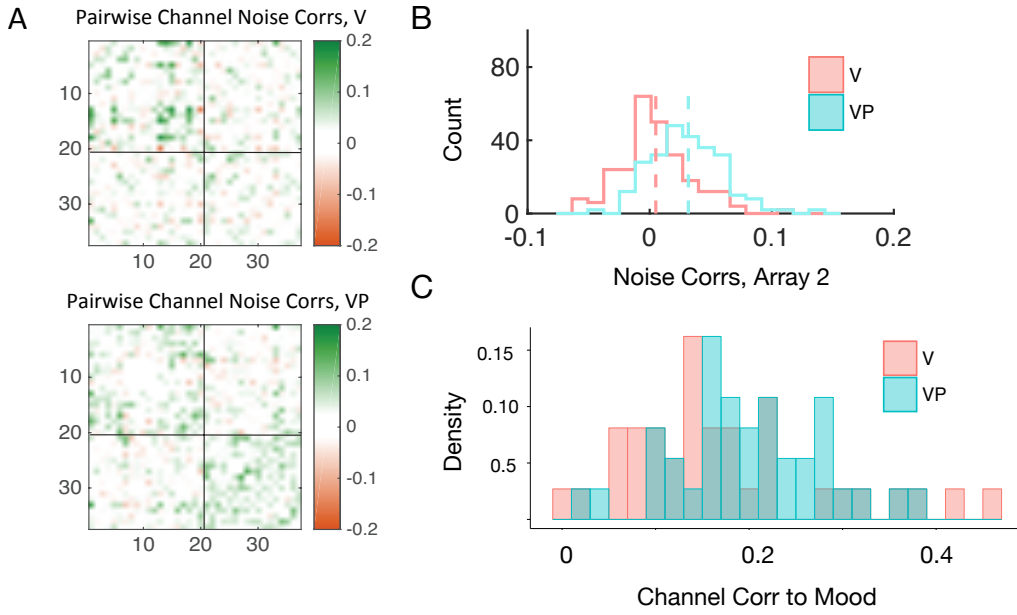
Figure 2.5: Low-dimensional shared variability in the VP condition **(a)** Pairwise noise correlations for paired day channels in the V (upper) and VP (lower) conditions. Channels are ordered according to their array locations, the black solid lines delineate the two electrode arrays. Array 2 consists of channels 21 through 38. **(b)** Distribution of noise correlations on Array 2. **(c)** Distribution of the correlation between the residuals of each channel on the paired day and the *mood* of the population, or the average residual activity as a function of time across channels. Channels are more correlated with the mood in the VP condition, indicating that noise fluctuations in the VP condition are shared by many channels.

probability that the same neurons were being recorded in feedback conditions (Figure C.1a-b). An anatomical mapping of noise correlations revealed that large, proximally-located subpopulations of channels on the microelectrode arrays co-fluctuated about their individual tuning curves in the VP condition. The VP condition was specifically marked by a significant increase in noise correlations on Array 2 of our MEAs (Figure C.1b, $p = 1.5 \times 10^{-19}$, two-sided Wilcoxon signed rank test). We characterized the *mood* of the neural population–the global, un-tuned activity as a function of time–using the average of the activity of the all N analyzed neurons after the spiking activity due to velocity tuning was removed. We then measured the correlation between each channel's residuals and the mood. Individual channels had greater correlation with the mood in the VP condition (Figure C.1c), indicating that there were global co-fluctuations in the noise in the VP condition.

2.4.3   A shared gain model of somatosensory feedback in M1

Our neural data analysis in Sections 2.4.1 and 2.4.2 revealed spiking co-variability in the VP condition that could not be explained by Equation 2.5, in which the spiking activity of each channel i was conditioned exclusively on its private velocity tuning. We developed a new model of M1 activity that quantifies global gain fluctuations in the VP condition. In the new model, the spiking activity of each channel i is conditioned on its private velocity tuning and a waveform of activity shared by every channel (Equation 2.7). The global waveform modulates the gain of each channel's private velocity tuning curve; the degree of that modulation is controlled by a term that represents the channel's coupling strength to the global activity. Examples of $\gamma(t)$ are shown in Figure 2.6. We were struck by the observation that $\gamma(t)$ seemed to fluctuate at time scales relevant to the duration of one imagined reach, despite the fact that we placed no constraint on our modulator's timescale (in our regression format, the temporal neighborhood of smoothing).

Moreover, when we compared the form of $\gamma(t)$ across reach epochs, we found that its latent, 1D dynamics were remarkably stereotyped across repeated reach trajectories (Figure 2.6b). Many potential factors could give rise to shared variability with stereotyped dynamics; proprioceptive information is one such factor that would be strongly correlated with reach type, as different subsets of muscle and tendon receptors are activated for reaches across body space. We are cautious of making bold claims about this observation, especially because we have very few repeated reaches for a given recording session. The form of $\gamma(t)$ fluctuations is probably not comparable across days, over which period it is unlikely that we are fitting our regression models to the same neural population across. Even if we were observing the same neurons over multiple recording sessions, we would likely need to account for population-wide slow drifts in neural activity to align $\gamma(t)$ over days [61, 96]. But slow drifts would share scaling with our formulation of $\gamma(t)$, making the two difficult to disambiguate. We hope future studies with more repeated reaching trials and statistical power might examine the latent dynamics of trial-to-trial variability in M1 to see if they have stereotyped form related to somatosensory feedback. Many studies have found evidence of latent manifolds that constrain M1's tuned activity during movement control [19, 97, 98], but few have isolated and examined the population structure of residual activity [58].
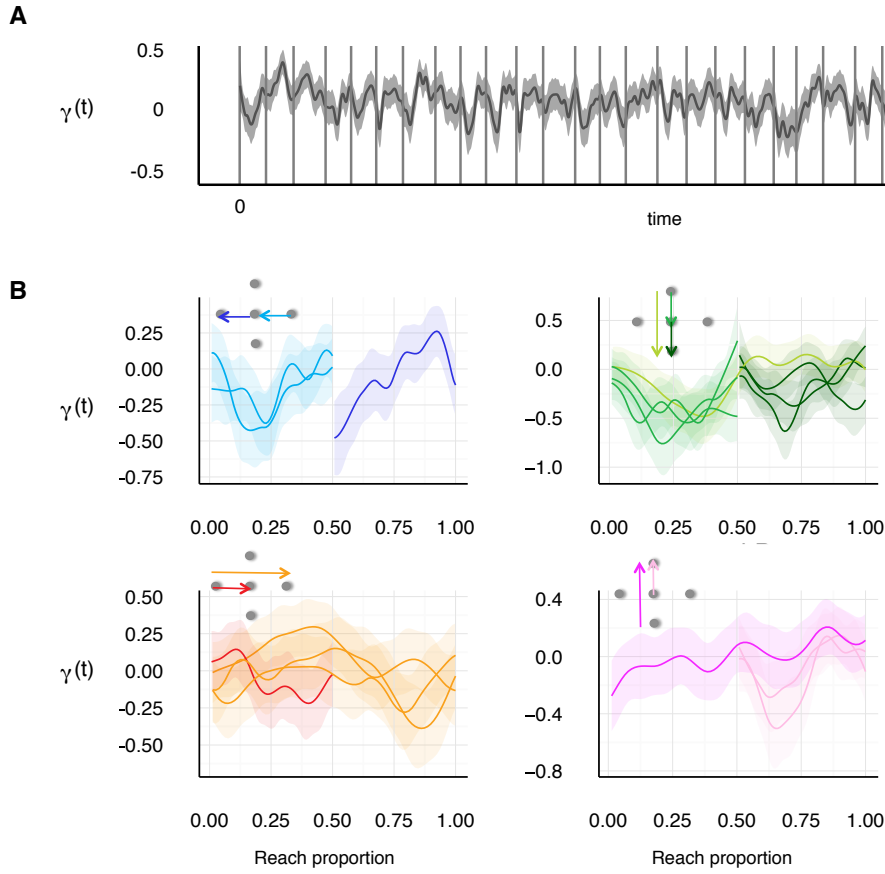
Figure 2.6: Latent shared gain trajectories $\gamma(t)$ in M1 trial-to-trial activity **(a)** Example of a shared gain signal $\gamma(t)$, fitted using the shared gain model in Equation 7. The entire time-course of $\gamma(t)$ across all 30 reaches is shown, where reach epochs are delineated with vertical lines. The confidence band represents a 95% CI. The regression is fitted with a log-link function, so negative values of $\gamma(t)$ are interpreted as gain depression. **(b)** Shared gain signal $\gamma(t)$ segmented by reach type. Confidence bands represent 95% CIs. On a single plot, reaches of the same type are shown in the same color. The type of reach is indicated by the corresponding target diagram in the upper lefthand corner of the plot. $\gamma(t)$ traces are aligned using reach proportion (x axis), which the fraction of the reach completed, where the completion of a reach across two targets in either the x or y direction has a value of 1.

The addition of a shared gain term improved model fits dramatically for both the V and VP condition. Figure 2.7 shows the adjusted R^2 of the entire tuned population for the cosine tuning model (Equation 2.5) and the shared gain model (Equation 2.7) in both the V and VP conditions. The shared gain term explains 54.9% and 33.9% more spiking variability on average in the V and VP conditions, respectively, where averages were computed across training sessions with the same feedback conditions. However, variability in results across training sessions were large, especially in the V condition.
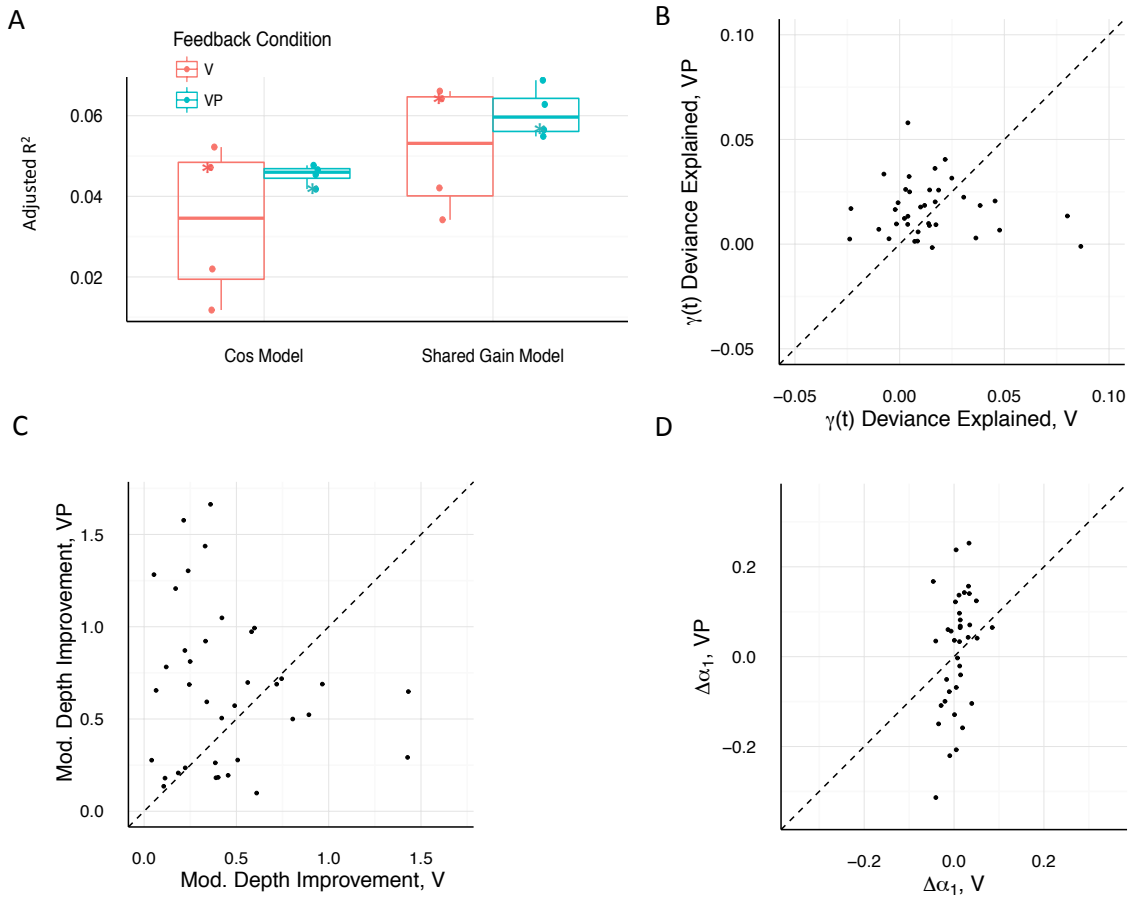
37

Figure 2.7: The shared gain model improves M1 tuning differentially in the VP condition. **(a)** Adjusted R^2 of the full population model (containing all N channels) for the V and VP conditions and the Cosine Tuning and Shared Gain models. Each point represents one analyzed training session, and there were four training sessions of each feedback condition. The paired day results are indicated with a *. Though the shared gain model assists tuning in both the V and VP conditions, the paired day shows more improvement for the VP than the V condition. **(b)** The proportion of deviance explained by $\gamma(t)$ for each channel i in the V and VP condition. Single channel values may be negative because all channels in the Shared Gain model are fit simultaneously (and the result will be the best fit for the entirety of the population). More deviance is explained by $\gamma(t)$ in the VP condition. **(c)** The improvement in the modulation depth of each channel i's velocity tuning after the addition of $\gamma(t)$, on the paired day. More channels show greater modulation depth improvement with the addition of $\gamma(t)$ in the VP condition. **(d)** Change in the amplitude (α_1, Eq. (2.6)) of velocity tuning for each channel i on the paired day with the addition of $\gamma(t)$. Channels show larger amplitude shifts in the VP condition, and therefore $\gamma(t)$ has greater effect.

We can also calculated the proportion of deviance explained explicitly by the shared gain term $\gamma(t)$ for each of the i fitted channels in a training session. On the paired day, the shared gain term explained a larger proportion of deviance in the VP condition than the V condition for 59.5% of channels (Figure 2.7b), indicating that $\gamma(t)$ aids the mapping between kinematics and spiking activity more in the VP than the V condition. Similarly, $\gamma(t)$ caused a differential increase in the modulation depth of channel tuning curves in the VP condition in 64.8% of channels (Figure 2.7c). This effect arises because the inclusion of a $\gamma(t)$ waveform causes much larger shifts in VP tuning curve parameters than V tuning curve parameters. With the addition of $\gamma(t)$, channels on the paired day showed larger standardized changes in the amplitude of their cosine velocity tuning curves (α_{i1}, Equation 2.6) in the VP condition than the V condition (Figure 2.7d). Together, these results suggest that global co-fluctuations of the neural population in the VP condition mask channels' private velocity tuning; once we condition spiking responses on a shared gain waveform $\gamma(t)$ in the VP condition, channels are more sharply tuned to endpoint velocity.

2.5 Discussion

We had the first known opportunity to study the neural differences between feedforward and closed-loop, somatosensory-assisted motor control in a human subject with a motor-specific neuropathy. We found that BMI-assisted motor control significantly degraded when there was a mismatch in the sensory feedback sources provided during decoder training and online BMI reaching performance. The change in motor behavior between the visual (V) and visual+proprioceptive (VP) conditions was marked neurally by significant shifts in the preferred directions, gains, and variability of M1 velocity tuning curves.

Our results are at odds with those of a previous study from Suminski et al. [87], which found that online proprioceptive feedback improved BMI-assisted reaching behavior in non-human primates even when the BMI decoder was trained with vision alone. The result from Suminski et al. [87] would require that M1 velocity tuning remain stable in the presence/absence of proprioceptive feedback, and that proprioception simply improve the signal-to-noise ratio of stable velocity tuning curves. Other studies have demonstrated instabilities in M1 tuning during

sensory adaptation [99] and motor learning [100], lending credence to our conclusion that the mapping from kinematics to spiking activity shifts in the presence of proprioception.

There are several notable differences between our experiment and that published by Suminski et al. [87], which could account for the contrasting results. First, the neural data in their study was automatically sorted by the voltage waveform of the recorded spikes to ensure that tuning models were fit to the activity of single neurons. We chose not to spike sort the activity of our recorded channels, in part due to research demonstrating that BMIs have trivial reductions in performance when channel activity is merely thresholded rather than sorted, and successful spike sorting requires large quantities of data collected at high sampling rates [101]. We also observed that very few channels of our recorded data had supra-threshold single-unit activity; spike sorting activity for single units would therefore remove much of the information we recorded from the M1 population. It is therefore possible that the shift in tuning that we observed in the VP condition could be do to the activation of different subsets of cells recorded by a single electrode, and not to a shift in the velocity preference of single neuron. However, this explanation would be much more likely if we observed preferred direction shifts on only a few channels; instead, we observed shifts $\geq$ 45 degrees on the majority of recorded channels. The non-human primate subjects in the Suminski et al. [87] study also had years of experience using visually-trained BMI decoders of the form used in the experiment. We consider it more likely that the M1 activity of the non-human primates had adapted to optimize that decoder output [91, 92, 93]; this adaptation may have masked natural representations of somatosensory information.

More unexpectedly, we found that proprioception degraded reaching performance even when subject used a decoder trained with proprioceptive feedback. This is an unintuitive result given several proposed neural models of Bayesian multisensory integration, which posit that sensory state estimation is achieved through a linear combination of the sensory feedback sources, with weights that are inversely proportional to the variance of the feedback source [102, 103]. In this framework, state estimation can only be as bad as the most variable sensory cue. One would therefore think that motor responses to simultaneous visual and proprioceptive feedback would be at least as reliable as motor responses to visual feedback alone. However, the behavioral consequence of sensory cue integration is dependent on the read-out of the circuit. Circuits native to or downstream of M1 may be able to effectively integrate visual and

somatosensory information such that additive proprioceptive feedback decreases the variability of motor output. Moreover, these read-out circuits may in fact be linearly summing basis patterns of activity encoded by visual and somatosensory feedback, but the basis patterns may not be of the tuning forms recognized by our current BMI decoder implementations.

Our results showed that a gain-modulating waveform of activity, which was shared across the M1 population, masked the effects of velocity tuning on spiking variability, particularly when M1 received somatosensory feedback. Our findings come amidst a series of recent publications that have discovered low-rank neural activity in several sensory regions of cortex [55, 22, 23]. These large network co-fluctuations have been shown to dominate and mask local circuit effects when their presence is not accounted for [72]. Though the co-fluctuations of activity uncovered by all of these studies are not due to the effects of the stimulus presented during the experiment, the mass coordination of the activity suggests that it is an effect of the circuit that shapes computation and not simply "noise".

Though the source or circuit mechanism of the gain-modulating signal in our model remains uncertain, there are reasons to believe the shared gain term could represent communication from S1 to M1. First, the shared gain model aids the tuning of neural data in the VP condition more than the V condition. Additionally, sensorimotor circuit research has shown evidence that M1 neurons most responsive to sensory information are intermingled with motor-tuned neurons [104]. Furthermore, despite the fact that the S1 tonotopy is roughly preserved in S1 to M1 projections [105, 106], S1 tonotopic projections terminate in overlapping regions of M1, and wide M1 neuron dendritic activity results in single M1 neurons integrating information from broad somatotopic regions of S1 [88]. Finally, previous studies has found evidence of traveling waves of correlated fluctuations between sensory and motor areas, which would not be dissimilar in form from our modeling choice of $\gamma(t)$ [107]. We do not rule out the possibility that the shared gain term in our model represents converging somatosensory input as well as other sources of network co-variability [96]. This could explain why a shared gain signal still aided M1 tuning in the V condition.

In its current form, our shared gain model of M1 tuning presents a few challenges for translation to clinical BMI work. Though it is straightforward to invert our tuning model and create an Optimal Linear Estimator (OLE) [108] that predicts velocity kinematics from the neural data,

doing so requires us to have advanced knowledge of the form of the shared gain signal over time. In other words, a decoder trained with one set of neural data might not have a shard gain signal that was generalizable to a new set of neural data encountered during online decoding. This challenge might be overcome if the single-trial activity of the shared gain signal has predictable dynamics, as suggested by our results in Figure 2.6. Additionally, the shared gain signal may be partially co-linear with velocity kinematics, meaning that neural data would contain less information about velocity once the effects of the shared gain were subtracted in the decoding process. Though just as others have espoused the benefits of using BMI as a tool for basic science research [109, 110], we view this study primarily as a rare opportunity to gain insight into human sensorimotor coding. Clinical BMI decoders that utilize somatosensory feedback will progress as we continue to gain a better understanding of the communication between S1 and M1.

Bibliography

[1] S. Herculano-Houzel. The human brain in numbers: a linearly scaled-up primate brain. *Frontiers in human neuroscience* **3**, 31 (2009).

[2] F. Rieke, D. Warland, R. D. R. Van Steveninck, W. S. Bialek et al. *Spikes: exploring the neural code*, volume 7 (MIT press Cambridge, 1999).

[3] A. Pouget, P. Dayan & R. Zemel. Information processing with population codes. *Nature Reviews Neuroscience* **1**(2), 125–132 (2000).

[4] R. Yuste. From the neuron doctrine to neural networks. *Nature reviews neuroscience* **16**(8), 487–497 (2015).

[5] D. A. Ruff, A. M. Ni & M. R. Cohen. Cognition as a window into neuronal population space. *Annual review of neuroscience* **41**, 77–97 (2018).

[6] M. D. Humphries. Dynamical networks: finding, measuring, and tracking neural population activity using network science. *Network Neuroscience* **1**(4), 324–338 (2017).

[7] I. H. Stevenson & K. P. Kording. How advances in neural recording affect data analysis. *Nature neuroscience* **14**(2), 139 (2011).

[8] P. Gao & S. Ganguli. On simplicity and complexity in the brave new world of large-scale neuroscience. *Current opinion in neurobiology* **32**, 148–155 (2015).

[9] G. Buzsáki. Large-scale recording of neuronal ensembles. *Nature neuroscience* **7**(5), 446–451 (2004).

[10] T. Schrödel, R. Prevedel, K. Aumayr, M. Zimmer & A. Vaziri. Brain-wide 3d imaging of neuronal activity in caenorhabditis elegans with sculpted light. *Nature methods* **10**(10), 1013 (2013).

[11] M. Z. Lin & M. J. Schnitzer. Genetically encoded indicators of neuronal activity. *Nature neuroscience* **19**(9), 1142 (2016).

[12] M. E. J. Obien, K. Deligkaris, T. Bullmann, D. J. Bakkum & U. Frey. Revealing neuronal function through microelectrode array recordings. *Frontiers in neuroscience* **8**, 423 (2015).

[13] G. Hong & C. M. Lieber. Novel electrode technologies for neural recordings. *Nature Reviews Neuroscience* **20**(6), 330–345 (2019).

[14] N. A. Steinmetz, C. Koch, K. D. Harris & M. Carandini. Challenges and opportunities for large-scale electrophysiology with neuropixels probes. *Current opinion in neurobiology* **50**, 92–100 (2018).

[15] S. Saxena & J. P. Cunningham. Towards the neural population doctrine. *Current opinion in neurobiology* **55**, 103–111 (2019).

[16] B. Doiron, A. Litwin-Kumar, R. Rosenbaum, G. K. Ocker & K. Josić. The mechanics of state-dependent neural correlations. *Nature neuroscience* **19**(3), 383 (2016).

[17] R. E. Kass et al. Computational neuroscience: Mathematical and statistical perspectives. *Annual review of statistics and its application* **5**, 183–214 (2018).

[18] A. Kohn, R. Coen-Cagli, I. Kanitscheider & A. Pouget. Correlations and neuronal population information. *Annual review of neuroscience* **39**, 237–256 (2016).

[19] J. A. Gallego, M. G. Perich, L. E. Miller & S. A. Solla. Neural manifolds for the control of movement. *Neuron* **94**(5), 978–984 (2017).

[20] S. Ganguli & H. Sompolinsky. Compressed sensing, sparsity, and dimensionality in neuronal information processing and data analysis. *Annu. Rev. Neurosci.* **35**(1), 485–508 (2012).

[21] J. P. Cunningham & M. Y. Byron. Dimensionality reduction for large-scale neural recordings. *Nature neuroscience* **17**(11), 1500 (2014).

[22] I.-C. Lin, M. Okun, M. Carandini & K. D. Harris. The nature of shared cortical variability. *Neuron* **87**(3), 644–656 (2015).

[23] N. C. Rabinowitz, R. L. Goris, M. Cohen & E. P. Simoncelli. Attention stabilizes the shared gain of v4 populations. *Elife* **4**, e08998 (2015).

[24] C. Huang et al. Circuit models of low-dimensional shared variability in cortical networks. *Neuron* **101**(2), 337–348 (2019).

[25] B. B. Averbeck, P. E. Latham & A. Pouget. Neural correlations, population coding and computation. *Nat. Rev. Neurosci.* **7**(5), 358–366 (2006).

[26] K. Josić, E. Shea-Brown, B. Doiron & J. de la Rocha. Stimulus-dependent correlations and population codes. *Neural computation* **21**(10), 2774–2804 (2009).

[27] A. Litwin-Kumar. *Relationship between neuronal architecture and variability in cortical circuits*. Ph.D. thesis, Carnegie Mellon University (2013).

[28] A. A. Faisal, L. P. Selen & D. M. Wolpert. Noise in the nervous system. *Nature reviews neuroscience* **9**(4), 292–303 (2008).

[29] R. Rosenbaum, J. E. Rubin & B. Doiron. Short-term synaptic depression and stochastic vesicle dynamics reduce and shape neuronal correlations. *Journal of neurophysiology* **109**(2), 475–484 (2013).

[30] A. D. Bird & M. J. Richardson. Long-term plasticity determines the postsynaptic response to correlated afferents with multivesicular short-term synaptic depression. *Frontiers in computational neuroscience* **8**, 2 (2014).

[31] J. F. A. Poulet & C. C. H. Petersen. Internal brain state regulates membrane potential synchrony in barrel cortex of behaving mice. *Nature* **454**(7206), 881–885 (2008).

[32] M. R. Cohen & J. H. R. Maunsell. Attention improves performance primarily by reducing interneuronal correlations. *Nat. Neurosci.* **12**(12), 1594–1600 (2009).

[33] J. F. Mitchell, K. A. Sundberg & J. H. Reynolds. Spatial attention decorrelates intrinsic activity fluctuations in macaque area V4. *Neuron* **63**(6), 879–888 (2009).

[34] J. Jeanne, T. Sharpee & T. Gentner. Associative learning enhances population coding by inverting interneuronal correlation patterns. *Neuron* **78**(2), 352–363 (2013).

[35] Y. Gu et al. Perceptual learning reduces interneuronal correlations in macaque visual cortex. *Neuron* **71**(4), 750–761 (2011).

[36] R. Salazar, N. Dotson, S. Bressler & C. Gray. Content-specific fronto-parietal synchronization during visual working memory. *Science* **338**(6110), 1097–1100 (2012).

[37] N. M. Dotson, R. F. Salazar & C. M. Gray. Frontoparietal correlation dynamics reveal interplay between integration and segregation during visual working memory. *Journal of Neuroscience* **34**(41), 13600–13613 (2014).

[38] M. Vidne et al. Modeling the impact of common noise inputs on the network activity of retinal ganglion cells. *Journal of computational neuroscience* **33**(1), 97–121 (2012).

[39] J. E. Kulkarni & L. Paninski. Common-input models for multiple neural spike-train data. *Network: Computation in Neural Systems* **18**(4), 375–407 (2007).

[40] S. Roweis & Z. Ghahramani. A unifying review of linear gaussian models. *Neural computation* **11**(2), 305–345 (1999).

[41] J. P. Cunningham & Z. Ghahramani. Linear dimensionality reduction: Survey, insights, and generalizations. *The Journal of Machine Learning Research* **16**(1), 2859–2900 (2015).

[42] M. Y. Byron et al. Gaussian-process factor analysis for low-dimensional single-trial analysis of neural population activity. In *Advances in neural information processing systems*, 1881–1888 (2009).

[43] S. Linderman et al. Bayesian learning and inference in recurrent switching linear dynamical systems. In *Artificial Intelligence and Statistics*, 914–922 (2017).

[44] M. Y. Byron et al. Extracting dynamical structure embedded in neural activity. In *Advances in neural information processing systems*, 1545–1552 (2006).

[45] R. E. Kass & V. Ventura. A spike-train probability model. *Neural computation* **13**(8), 1713–1720 (2001).

[46] L. Paninski, J. Pillow & J. Lewi. Statistical models for neural encoding, decoding, and optimal stimulus design. *Progress in brain research* **165**, 493–507 (2007).

[47] A. C. Smith & E. N. Brown. Estimating a state-space model from point process observations. *Neural computation* **15**(5), 965–991 (2003).

[48] W. Truccolo, U. T. Eden, M. R. Fellows, J. P. Donoghue & E. N. Brown. A point process framework for relating neural spiking activity to spiking history, neural ensemble, and extrinsic covariate effects. *Journal of neurophysiology* **93**(2), 1074–1089 (2005).

[49] L. Srinivasan, U. T. Eden, A. S. Willsky & E. N. Brown. A state-space analysis for reconstruction of goal-directed movements using neural signals. *Neural computation* **18**(10), 2465–2494 (2006).

[50] B. M. Yu et al. Mixture of trajectory models for neural decoding of goal-directed movements. *Journal of neurophysiology* **97**(5), 3763–3780 (2007).

[51] V. Lawhern, W. Wu, N. Hatsopoulos & L. Paninski. Population decoding of motor cortical activity using a generalized linear model with hidden states. *Journal of neuroscience methods* **189**(2), 267–280 (2010).

[52] L. Paninski et al. A new look at state-space models for neural data. *Journal of computational neuroscience* **29**(1-2), 107–126 (2010).

[53] S. W. Linderman & S. J. Gershman. Using computational theory to constrain statistical models of neural data. *Current opinion in neurobiology* **46**, 14–24 (2017).

[54] M. L. Schölvinck, A. B. Saleem, A. Benucci, K. D. Harris & M. Carandini. Cortical state determines global variability and correlations in visual cortex. *Journal of Neuroscience* **35**(1), 170–178 (2015).

[55] M. Okun et al. Diverse coupling of neurons to populations in sensory cortex. *Nature* **521**(7553), 511–515 (2015).

[56] M. Vidne et al. Inferring functional connectivity in an ensemble of retinal ganglion cells sharing a common input. In *Frontiers in systems neuroscience conference abstract: Computational and systems neuroscience 2009* (2009).

[57] W. Wu, J. E. Kulkarni, N. G. Hatsopoulos & L. Paninski. Neural decoding of hand motion using a linear state-space model with hidden states. *IEEE Transactions on neural systems and rehabilitation engineering* **17**(4), 370–378 (2009).

[58] R. C. Williamson, B. Doiron, M. A. Smith & M. Y. Byron. Bridging large-scale neuronal recordings and large-scale network models using dimensionality reduction. *Current opinion in neurobiology* **55**, 40–47 (2019).

[59] R. C. Williamson et al. Scaling properties of dimensionality reduction for neural populations and network models. *PLoS computational biology* **12**(12) (2016).

[60] A. Litwin-Kumar & B. Doiron. Slow dynamics and high variability in balanced cortical networks with clustered connections. *Nat. Neurosci.* **15**(11), 1498–1505 (2012).

[61] B. R. Cowley et al. Slow drift of neural activity as a signature of impulsivity in macaque visual and prefrontal cortex. *bioRxiv* (2020).

[62] C. van Vreeswijk & H. Sompolinsky. Chaos in neuronal networks with balanced excitatory and inhibitory activity. *Science* **274**(5293), 1724–1726 (1996).

[63] C. van Vreeswijk & H. Sompolinsky. Chaotic balanced state in a model of cortical circuits. *Neural Comput.* **10**(6), 1321–1371 (1998).

[64] A. Renart et al. The asynchronous state in cortical circuits. *Science* **327**(5965), 587–590 (2010).

[65] A. Litwin-Kumar, A.-M. M. Oswald, N. N. Urban & B. Doiron. Balanced synaptic input shapes the correlation between neural spike trains. *PLoS Comput. Biol.* **7**(12), e1002305 (2011).

[66] F. S. Chance, L. Abbott & A. D. Reyes. Gain modulation from background synaptic input. *Neuron* **35**(4), 773–782 (2002).

[67] J. A. Cardin, L. A. Palmer & D. Contreras. Cellular mechanisms underlying stimulus-dependent gain modulation in primary visual cortex neurons in vivo. *Neuron* **59**(1), 150–160 (2008).

[68] M. T. Schaub, Y. N. Billeh, C. A. Anastassiou, C. Koch & M. Barahona. Emergence of slow-switching assemblies in structured neuronal networks. *PLoS computational biology* **11**(7) (2015).

[69] B. Kriener, M. Helias, A. Aertsen & S. Rotter. Correlations in spiking neuronal networks with distance dependent connections. *J. Comput. Neurosci.* **27**(2), 177–200 (2009).

[70] A. Keane & P. Gong. Propagating waves can explain irregular neural dynamics. *Journal of Neuroscience* **35**(4), 1591–1605 (2015).

[71] R. Rosenbaum & B. Doiron. Balanced networks of spiking neurons with spatially dependent recurrent connections. *Physical Review X* **4**(2), 021039 (2014).

[72] R. Rosenbaum, M. A. Smith, A. Kohn, J. E. Rubin & B. Doiron. The spatial structure of correlated neuronal variability. *Nature neuroscience* **20**(1), 107 (2017).

[73] S. H. Scott. Optimal feedback control and the neural basis of volitional motor control. *Nature Reviews Neuroscience* **5**(7), 532–545 (2004).

[74] J. Wright, V. G. Macefield, A. van Schaik & J. C. Tapson. A review of control strategies in closed-loop neuroprosthetic systems. *Frontiers in neuroscience* **10**, 312 (2016).

[75] N. Li, T.-W. Chen, Z. V. Guo, C. R. Gerfen & K. Svoboda. A motor cortex circuit for motor planning and movement. *Nature* **519**(7541), 51–56 (2015).

[76] A. P. Georgopoulos, J. F. Kalaska, R. Caminiti & J. T. Massey. On the relations between the direction of two-dimensional arm movements and cell discharge in primate motor cortex. *The Journal of Neuroscience* **2**(11), 1527–1537 (1982).

[77] K. Pipereit, O. Bock & J.-L. Vercher. The contribution of proprioceptive feedback to sensorimotor adaptation. *Experimental Brain Research* **174**(1), 45 (2006).

[78] C. Ghez, J. Gordon & M. F. Ghilardi. Impairments of reaching movements in patients without proprioception. ii. effects of visual information on accuracy. *Journal of neurophysiology* **73**(1), 361–372 (1995).

[79] J. Cole & J. Paillard. Living without touch and peripheral information about body position and movement: Studies with deafferented subjects. *The body and the self* 245–266 (1995).

[80] J. Paillard. Body schema and body image-a double dissociation. *Motor control, today and tomorrow* 197–214 (1999).

[81] F. Matyas et al. Motor control by sensory cortex. *Science* **330**(6008), 1240–1243 (2010).

[82] S. Sachidhanandam, V. Sreenivasan, A. Kyriakatos, Y. Kremer & C. C. Petersen. Membrane potential correlates of sensory perception in mouse barrel cortex. *Nature neuroscience* **16**(11), 1671–1677 (2013).

[83] A. B. Schwartz, X. T. Cui, D. J. Weber & D. W. Moran. Brain-controlled interfaces: movement restoration with neural prosthetics. *Neuron* **52**(1), 205–220 (2006).

[84] S. J. Bensmaia & L. E. Miller. Restoring sensorimotor function through intracortical interfaces: progress and looming challenges. *Nature Reviews Neuroscience* **15**(5), 313–325 (2014).

[85] S. C. Gandevia, K. M. Refshauge & D. F. Collins. Proprioception: peripheral inputs and perceptual interactions. In *Sensorimotor control of movement and posture*, 61–68 (Springer, 2002).

[86] R. Johansson & Å. B. Vallbo. Detection of tactile stimuli. thresholds of afferent units related to psychophysical thresholds in the human hand. *The Journal of physiology* **297**, 405 (1979).

[87] A. J. Suminski, D. C. Tkach, A. H. Fagg & N. G. Hatsopoulos. Incorporating feedback from multiple sensory modalities enhances brain–machine interface control. *The Journal of neuroscience* **30**(50), 16777–16787 (2010).

[88] B. M. Hooks, J. Y. Lin, C. Guo & K. Svoboda. Dual-channel circuit mapping reveals sensorimotor convergence in the primary motor cortex. *The Journal of Neuroscience* **35**(10), 4418–4426 (2015).

[89] J. L. Collinger et al. High-performance neuroprosthetic control by an individual with tetraplegia. *The Lancet* **381**(9866), 557–564 (2013).

[90] W. Wang, S. S. Chan, D. A. Heldman & D. W. Moran. Motor cortical representation of position and velocity during reaching. *Journal of neurophysiology* **97**(6), 4258–4270 (2007).

[91] M. A. Lebedev et al. Cortical ensemble adaptation to represent velocity of an artificial actuator controlled by a brain-machine interface. *The Journal of neuroscience* **25**(19), 4681–4693 (2005).

[92] B. Jarosiewicz et al. Functional network reorganization during learning in a brain-computer interface paradigm. *Proceedings of the National Academy of Sciences* **105**(49), 19486–19491 (2008).

[93] K. Ganguly & J. M. Carmena. Emergence of a stable cortical map for neuroprosthetic control. *PLoS Biol* **7**(7), e1000153 (2009).

[94] T. Hastie & R. Tibshirani. Generalized additive models. *Statistical science* 297–310 (1986).

[95] J. Fan, N. E. Heckman & M. P. Wand. Local polynomial kernel regression for generalized linear models and quasi-likelihood functions. *Journal of the American Statistical Association* **90**(429), 141–150 (1995).

[96] R. L. Goris, J. A. Movshon & E. P. Simoncelli. Partitioning neuronal variability. *Nature neuroscience* **17**(6), 858 (2014).

[97] G. F. Elsayed, A. H. Lara, M. T. Kaufman, M. M. Churchland & J. P. Cunningham. Reorganization between preparatory and movement population responses in motor cortex. *Nature communications* **7**(1), 1–15 (2016).

[98] P. T. Sadtler et al. Neural constraints on learning. *Nature* **512**(7515), 423–426 (2014).

[99] Y. Mandelblat-Cerf, R. Paz & E. Vaadia. Trial-to-trial variability of single cells in motor cortices is dynamically modified during visuomotor adaptation. *The Journal of Neuroscience* **29**(48), 15053–15062 (2009).

[100] U. Rokni, A. G. Richardson, E. Bizzi & H. S. Seung. Motor learning with unstable neural representations. *Neuron* **54**(4), 653–666 (2007).

[101] B. P. Christie et al. Comparison of spike sorting and thresholding of voltage waveforms for intracortical brain-machine interface performance. *Journal of Neural Engineering* **12**(1), 016009 (2015).

[102] W. J. Ma, J. M. Beck, P. E. Latham & A. Pouget. Bayesian inference with probabilistic population codes. *Nature neuroscience* **9**(11), 1432–1438 (2006).

[103] C. R. Fetsch, A. Pouget, G. C. DeAngelis & D. E. Angelaki. Neural correlates of reliability-based cue weighting during multisensory integration. *Nature neuroscience* **15**(1), 146–154 (2012).

[104] D. Huber et al. Multiple dynamic representations in the motor cortex during sensorimotor learning. *Nature* **484**(7395), 473–478 (2012).

[105] R. Aronoff et al. Long-range connectivity of mouse primary somatosensory barrel cortex. *European Journal of Neuroscience* **31**(12), 2221–2233 (2010).

[106] T. Mao et al. Long-range neuronal circuits underlying the interaction between sensory and motor cortex. *Neuron* **72**(1), 111–123 (2011).

[107] I. Ferezou et al. Spatiotemporal dynamics of cortical sensorimotor integration in behaving mice. *Neuron* **56**(5), 907–923 (2007).

[108] S. M. Chase, A. B. Schwartz & R. E. Kass. Bias, optimal linear estimation, and the differences between open-loop simulation and closed-loop performance of spiking-based brain–computer interface algorithms. *Neural networks* **22**(9), 1203–1213 (2009).

[109] M. D. Golub, S. M. Chase, A. P. Batista & M. Y. Byron. Brain–computer interfaces for dissecting cognitive processes underlying sensorimotor control. *Current opinion in neurobiology* **37**, 53–58 (2016).

[110] K. E. Schroeder & C. A. Chestek. Intracortical brain-machine interfaces advance sensorimotor neuroscience. *Frontiers in Neuroscience* **10**, 291 (2016).

[111] M. N. Shadlen & W. T. Newsome. Noise, neural codes and cortical organization. *Curr. Opin. Neurobiol.* **4**(4), 569–579 (1994).

[112] T. P. Vogels & L. F. Abbott. Signal propagation and logic gating in networks of integrate-and-fire neurons. *J. Neurosci.* **25**(46), 10786 –10795 (2005).

[113] M. R. Cohen & A. Kohn. Measuring and interpreting neuronal correlations. *Nat. Neurosci.* **14**(7), 811–819 (2011).

[114] A. Kohn, A. Zandvakili & M. A. Smith. Correlations and brain states: from electrophysiology to functional imaging. *Curr. Opin. Neurobiol.* **19**(4), 434–438 (2009).

[115] A. S. Ecker et al. State dependence of noise correlations in macaque primary visual cortex. *Neuron* **82**(1), 235–248 (2014).

[116] R. Pyle & R. Rosenbaum. Spatiotemporal dynamics and reliable computations in recurrent spiking neural networks. *Physical review letters* **118**(1), 018103 (2017).

[117] R. Darshan, C. Van Vreeswijk & D. Hansel. Strength of correlations in strongly recurrent neuronal networks. *Physical Review X* **8**(3), 031072 (2018).

[118] Y. Hu, J. Trousdale, K. Josić & E. Shea-Brown. Motif statistics and spike correlations in neuronal networks. *Journal of Statistical Mechanics: Theory and Experiment* **2013**(03), P03012 (2013).

[119] Y. Hu, J. Trousdale, K. Josić & E. Shea-Brown. Local paths to global coherence: cutting networks down to size. *Physical Review E* **89**(3), 032802 (2014).

[120] J. Trousdale, Y. Hu, E. Shea-Brown & K. Josić. Impact of network structure and cellular response on spike time correlations. *PLoS computational biology* **8**(3) (2012).

[121] V. Pernice, B. Staude, S. Cardanobile & S. Rotter. How structure determines correlations in neuronal networks. *PLoS computational biology* **7**(5) (2011).

[122] G. K. Ocker, K. Josić, E. Shea-Brown & M. A. Buice. Linking structure and activity in nonlinear spiking networks. *PLoS computational biology* **13**(6), e1005583 (2017).

[123] F. Mastrogiuseppe & S. Ostojic. Linking connectivity, dynamics, and computations in low-rank recurrent neural networks. *Neuron* **99**(3), 609 – 623.e29 (2018).

[124] Y. Ahmadian, F. Fumarola & K. D. Miller. Properties of networks with partially structured and partially random connectivity. *Physical Review E* **91**(1), 012820 (2015).

[125] S. Recanatesi, G. K. Ocker, M. A. Buice & E. Shea-Brown. Dimensionality in recurrent spiking networks: global trends in activity and local origins in connectivity. *PLoS computational biology* **15**(7), e1006446 (2019).

[126] A. Ponce-Alvarez, A. Thiele, T. D. Albright, G. R. Stoner & G. Deco. Stimulus-dependent variability and noise correlations in cortical mt neurons. *Proceedings of the National Academy of Sciences* **110**(32), 13162–13167 (2013).

[127] K. Wimmer et al. Sensory integration dynamics in a hierarchical network explains choice probabilities in cortical area mt. *Nature communications* **6**(1), 1–13 (2015).

[128] T. Kanashiro, G. K. Ocker, M. R. Cohen & B. Doiron. Attentional modulation of neuronal variability in circuit models of cortex. *Elife* **6**, e23978 (2017).

[129] G. Hennequin, Y. Ahmadian, D. B. Rubin, M. Lengyel & K. D. Miller. The dynamical regime of sensory cortex: stable dynamics around a single stimulus-tuned attractor account for patterns of noise variability. *Neuron* **98**(4), 846–860 (2018).

[130] D. Pandya & E. Yeterian. Comparison of prefrontal architecture and connections. *Philosophical Transactions of the Royal Society of London. Series B: Biological Sciences* **351**(1346), 1423–1432 (1996).

[131] C. H. Donahue & D. Lee. Dynamic routing of task-relevant signals for decision making in dorsolateral prefrontal cortex. *Nature neuroscience* **18**(2), 295 (2015).

[132] M. Siegel, T. J. Buschman & E. K. Miller. Cortical information flow during flexible sensorimotor decisions. *Science* **348**(6241), 1352–1355 (2015).

[133] J. M. Fuster. The prefrontal cortex—an update: time is of the essence. *Neuron* **30**(2), 319–333 (2001).

[134] S. B. Khanna, J. A. Scott & M. A. Smith. Dynamic shifts of visual and saccadic signals in prefrontal cortical regions 8ar and fef. *bioRxiv* 817478 (2019).

[135] G. Santhanam et al. Factor-analysis methods for higher-performance neural prostheses. *Journal of neurophysiology* **102**(2), 1315–1330 (2009).

[136] B. Everett. *An introduction to latent variable models* (Springer Science & Business Media, 2013).

[137] M. Bastian, S. Heymann & M. Jacomy. Gephi: An open source software for exploring and manipulating networks (2009).

[138] T. M. J. Fruchterman & E. M. Reingold. Graph drawing by force-directed placement. *Software: Practice and Experience* **21**(11), 1129–1164 (1991).

[139] B. Lindner, B. Doiron & A. Longtin. Theory of oscillatory firing induced by spatially correlated noise and delayed inhibitory feedback. *Phys. Rev. E* **72**(6), 061919 (2005).

[140] C. Baker, C. Ebsch, I. Lampl & R. Rosenbaum. Correlated states in balanced neuronal networks. *Physical Review E* **99**(5), 052414 (2019).

[141] A. P. Dempster, N. M. Laird & D. B. Rubin. Maximum likelihood from incomplete data via the em algorithm. *Journal of the Royal Statistical Society: Series B (Methodological)* **39**(1), 1–22 (1977).

[142] S. Funahashi, C. J. Bruce & P. S. Goldman-Rakic. Mnemonic coding of visual space in the monkey's dorsolateral prefrontal cortex. *Journal of neurophysiology* **61**(2), 331–349 (1989).

[143] H. Suzuki & M. Azuma. Topographic studies on visual neurons in the dorsolateral prefrontal cortex of the monkey. *Experimental brain research* **53**(1), 47–58 (1983).

[144] A. Mikami, S. Ito & K. Kubota. Visual response properties of dorsolateral prefrontal neurons during visual fixation task. *Journal of neurophysiology* **47**(4), 593–605 (1982).

[145] E. H. Yeterian, D. N. Pandya, F. Tomaiuolo & M. Petrides. The cortical connectivity of the prefrontal cortex in the monkey brain. *Cortex* **48**(1), 58–81 (2012).

[146] L. G. Ungerleider, T. W. Galkin, R. Desimone & R. Gattass. Cortical connections of area v4 in the macaque. *Cerebral Cortex* **18**(3), 477–499 (2008).

[147] M. L. Leavitt, F. Pieper, A. J. Sachs & J. C. Martinez-Trujillo. A quadrantic bias in prefrontal representation of visual-mnemonic space. *Cerebral Cortex* **28**(7), 2405–2421 (2018).

[148] D. A. Pollen, A. W. Przybyszewski, M. A. Rubin & W. Foote. Spatial receptive field organization of macaque v4 neurons. *Cerebral Cortex* **12**(6), 601–616 (2002).

[149] B. Doiron, B. Lindner, A. Longtin, L. Maler & J. Bastian. Oscillatory activity in electrosensory neurons increases with the spatial correlation of the stochastic input stimulus. *Phys. Rev. Lett.* **93**(4), 048101 (2004).

[150] S. Song, P. J. Sjöström, M. Reigl, S. Nelson & D. B. Chklovskii. Highly nonrandom features of synaptic connectivity in local cortical circuits. *PLoS Biol.* **3**(3), e68 (2005).

[151] R. Perin, T. K. Berger & H. Markram. A synaptic organizing principle for cortical neuronal groups. *PNAS* **108**(13), 5419 –5424 (2011).

[152] H. Ko et al. Functional specificity of local synaptic connections in neocortical networks. *Nature* **473**(7345), 87–91 (2011).

[153] J. L. Chen et al. Clustered dynamics of inhibitory synapses and dendritic spines in the adult neocortex. *Neuron* **74**(2), 361–373 (2012).

[154] R. D. D'Souza, P. Bista, A. M. Meier, W. Ji & A. Burkhalter. Spatial clustering of inhibition in mouse primary visual cortex. *Neuron* **104**(3), 588–600 (2019).

[155] M. M. Churchland et al. Stimulus onset quenches neural variability: a widespread cortical phenomenon. *Nat. Neurosci.* **13**(3), 369–378 (2010).

[156] A. K. Churchland et al. Variance as a signature of neural computations during decision making. *Neuron* **69**(4), 818–831 (2011).

[157] D. R. Cox & V. Isham. *Point processes* (CRC Press, 1980).

[158] C. K. Kim, A. Adhikari & K. Deisseroth. Integration of optogenetics with complementary methodologies in systems neuroscience. *Nature Reviews Neuroscience* **18**(4), 222 (2017).

[159] S. W. Linderman et al. Recurrent switching linear dynamical systems. *arXiv preprint arXiv:1610.08466* (2016).

[160] M. Rigotti et al. The importance of mixed selectivity in complex cognitive tasks. *Nature* **497**(7451), 585–590 (2013).

[161] T. Hofmann, B. Schölkopf & A. J. Smola. Kernel methods in machine learning. *The annals of statistics* 1171–1220 (2008).

[162] C. Gardiner. A handbook for the natural and social sciences. *Springer Series in Synergetics* **13** (2009).

[163] G. K. Ocker & B. Doiron. Kv7 channels regulate pairwise spiking covariability in health and disease. *Journal of neurophysiology* **112**(2), 340–352 (2014).